

# A finite volume method for multicomponent gas transport in a porous fuel cell electrode

John M. Stockie<sup>1,\*</sup>, Keith Promislow<sup>2,†</sup> and Brian R. Wetton<sup>3,‡</sup>

<sup>1</sup> Department of Mathematics and Statistics, University of New Brunswick, Fredericton, NB, Canada, E3B 5A3

<sup>2</sup> Department of Mathematics and Statistics, Simon Fraser University, Burnaby, BC, Canada, V5A 1S6

<sup>3</sup> Department of Mathematics, University of British Columbia, Vancouver, BC, Canada, V6T 1Z2

## SUMMARY

We present a mathematical model for multicomponent gas transport in an anisotropic fuel cell electrode. The model couples the Maxwell-Stefan equations for multicomponent diffusion along with Darcy's law for flow in a porous medium. The equations are discretized using a finite volume approach with the method of lines, and the resulting nonlinear system of differential equations is integrated in time using a stiff ODE solver. Numerical simulations are performed to validate the model and to investigate the effect of various parameters on fuel cell performance. Copyright © 2003 John Wiley & Sons, Ltd.

KEY WORDS: multicomponent transport, fuel cells, convection–diffusion, porous medium, finite volume method, stiff systems

## 1. Introduction

Proton exchange membrane (or PEM) fuel cells operate by combining oxygen and hydrogen in the presence of a platinum catalyst, which generates an electrical current and releases water as a by-product. A critical component of such fuel cells is the electrode, known in the fuel cell community as a *gas diffusion layer* or GDL, which is a very thin layer of porous carbon fiber paper lying on either side of the membrane. The consumption of reactant gases ( $H_2$  and  $O_2$ ) and generation of end products ( $H_2O$ ) create gradients in component concentrations across the thickness of the paper. Consequently, the flow of gases in the GDL is governed by a combination of convection, which governs the motion of

---

\* Correspondence to: J. M. Stockie, Department of Mathematics and Statistics, University of New Brunswick, P. O. Box 4400, Fredericton, NB, Canada, E3B 5A3. E-mail: stockie@unb.ca.

† E-mail: kpromisl@sfu.ca.

‡ E-mail: wetton@math.ubc.ca.

Contract/grant sponsor: Funding for this research was provided by grants from Ballard Power Systems and the MITACS Network of Centres of Excellence.

the mixture through the porous medium, and multicomponent diffusion of the reacting and non-reacting gas species relative to the convection.

In a previous paper [20], the first and second authors developed a mathematical model for gas transport in PEM fuel cells. The resulting coupled system of nonlinear diffusion equations possesses a convective time scale which is much faster than the diffusive one. This model is distinguished from similar multicomponent problems appearing in the groundwater transport and reservoir simulation literature (e.g., [7, 23]) due to the thinness of the domain and the high porosity of the GDL, which combine to give very different scalings of the solution variables. The vast majority of other fuel cell models appearing in the literature (e.g., [10, 21]) emphasize the complex coupling between mass, heat, and charge transport among the different components of a cell, while often simplifying certain aspects of the GDL. We take a different approach and focus our attention solely on mass transport in the GDL which is known to be a major factor influencing fuel cell performance [28]. This model may also be applied to other industrial and biological applications in which gas transport takes place across a very thin porous material, such as kiln drying of wood and humid gas flow in insulation [25, 27].

In this paper, we present an extension of the two-component model developed in [20] to gas mixtures containing three components. This is more realistic for our fuel cell application, where the non-reacting gas components are known to have a significant effect on diffusive transport. We develop a second order numerical scheme using a finite volume discretization in space, which requires careful handling of the nonlinear, reactive, boundary conditions in order to maintain full second-order accuracy. This problem is distinguished by a high level of numerical stiffness, which requires the use of implicit time-stepping. We have implemented an implicit, stiff solver based on Backward Differentiation Formulas, which has proven to be very effective. We also perform a sensitivity study that identifies certain geometrical and operational parameters that are critical to fuel cell performance. In particular, we study the effects of anisotropy and spatial inhomogeneity in the porous electrode material which arises due to the fibrous nature of the carbon fiber paper that makes up the GDL. This has not been investigated before in the context of fuel cells.

## 2. Mathematical Model

### 2.1. Overview of Fuel Cell Physics

A cross-sectional view through a PEM fuel cell is depicted in Fig. 1. The *membrane electrode assembly* or MEA is sandwiched between two graphite plates (shaded on the left half of the diagram) into which are etched flow channels for carrying oxygen gas in the cathode and hydrogen in the anode. We introduce a coordinate system in which  $x$  denotes distance along the horizontal direction in the MEA,  $y$  is measured along the height of a channel through the thickness of the MEA, and  $z$  denotes distance along the length of a flow channel.

Inside the channels, pressure gradients in the  $z$ -direction initiate the flow of gases along the channel, although these variations in  $z$  are quite slow. Furthermore, consumption of reactants and generation of end products lead to gradients in component concentrations within the  $x, y$ -plane. At the heart of the fuel cell is the *proton exchange membrane* or PEM, composed of a polymer material that is permeable

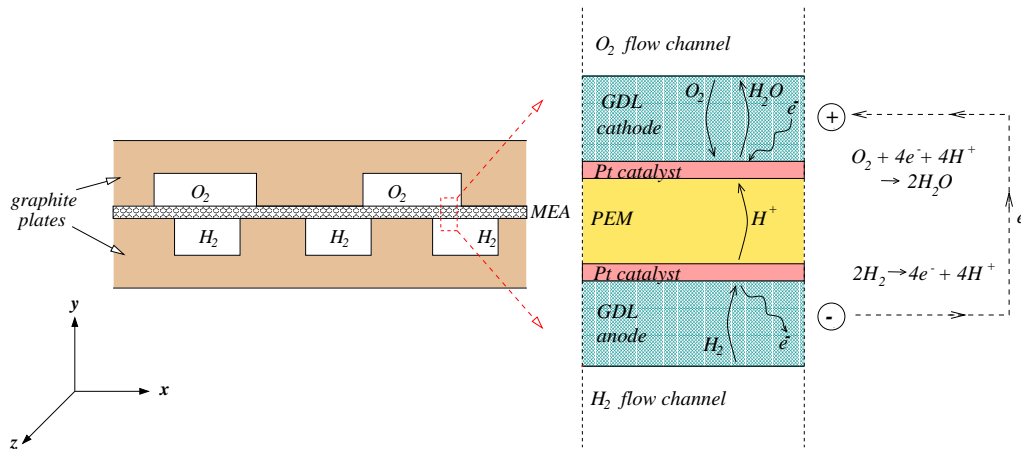


Figure 1. A proton exchange membrane fuel cell and its component parts. On the left is a cross-sectional view of the cell, showing the MEA sandwiched between the oxygen and hydrogen flow channels. The in-channel gas flow is directed normal to the page. On the right is a close-up view of the MEA. The reaction occurring at each electrode is listed on the far right, along with the flow of electrons generated when the anode and cathode are linked in an external circuit.

to small, positively-charged ions. On each side of the PEM is attached a layer of carbon fiber paper (the GDL) and the interface between the two is loaded with a platinum catalyst that facilitates the reactions. The primary purposes of the GDL are to provide a solid support for the catalyst particles and to distribute reactant gases uniformly to the catalyst layer. The electric current in a fuel cell is derived from the two reactions listed on the right of Fig. 1. Hydrogen ions liberated at the anode migrate across the PEM (driven by concentration gradients acting against the electrostatic forces) where they react with oxygen gas at the cathode catalyst layer to produce water vapor. The GDL and graphite plates are both conducting materials, and usable current is generated when the two electrodes are connected together in an external circuit.

## 2.2. Governing equations

We will focus our attention on isothermal, multispecies convective and diffusive transport in the GDL, extending the model derived in [20] in three significant ways:

- replacing the molar-averaged mixture velocity from Darcy's Law with a mass-averaged value. This is consistent with the mass transport literature (e.g., [3, 5, 17, 26]).
- adding the full dynamics of a third, non-reactive gas component to more accurately describe typical gas mixtures in fuel cells.
- using the Maxwell-Stefan equations for diffusive fluxes instead of Fick's Law. These equations are considered to be a more appropriate model for multicomponent diffusion [13]. Indeed, Amali et al. [2] present numerical evidence that in some situations Fick's Law underestimates the fluxes

for multicomponent transport in porous media by 5–10%.

For completeness, we summarize the derivation of the equations and boundary conditions below, and refer the interested reader to [20] for a more detailed treatment including a discussion of assumptions.

We consider each electrode in isolation and so our model domain is the two-dimensional cross-section through the GDL, labeled  $\Omega$  in Fig. 2. The lower boundary of  $\Omega$ , at  $y = 0$ , represents the

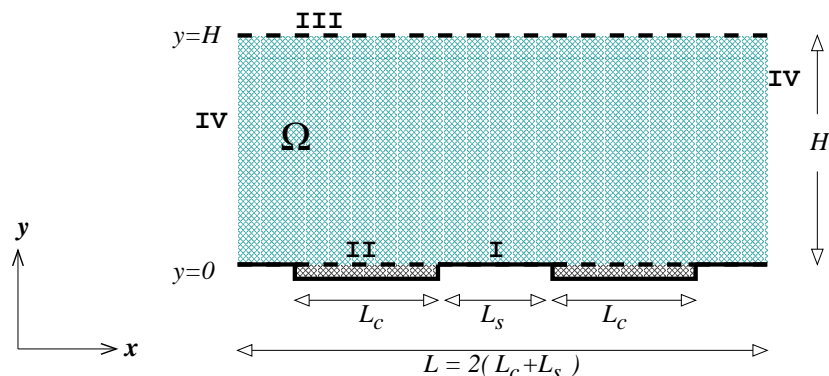


Figure 2. Dimensions of the model domain  $\Omega$ : GDL thickness  $H$ , channel width  $L_c$ , separation distance  $L_s$ , and total width  $L = 2(L_c + L_s)$ . The boundary components are identified by Roman numerals I–IV.

interface between the GDL and either the solid graphite plate or an open, gas-filled, flow channel. The upper boundary, at  $y = H$ , corresponds to the catalyst layer separating the GDL and the PEM. Each channel has a width of  $L_c$  and is separated from the next channel by a solid *landing area* of width  $L_s$ . The transport of ions and liquid water within the membrane-electrode assembly as well as the convective flow within the gas channels will not be modeled here. The coupling of the GDL to the rest of the fuel cell, including such effects as variation in reactant concentration along the length of the flow channel, nonuniformity of component concentrations in the channel, boundary layers at the porous GDL–channel interface, and dissociation rates at the catalyst layer will be relegated to boundary conditions.

The channel gases are typically humidified, and so we take the mixtures to be composed of three components: namely, humidified air at the cathode (oxygen, water vapor and nitrogen) and humidified hydrogen at the anode (consisting of hydrogen, water vapor and carbon dioxide). In addition to ignoring condensation and transport of heat and charge, we assume further that the gas mixtures are ideal and isothermal. Operation of fuel cells is known to be relatively independent of orientation and so we also neglect the force of gravity.

We now summarize the governing equations for the gas mixture, described by the individual component concentrations. Here we generalize the Fickian model employed in [20] to ternary gas mixtures, following the development in [3, 16]. We denote by  $C_1$  the reactant molar concentration, which is  $H_2$  on the anode side and  $O_2$  at the cathode. For both electrodes,  $C_2$  refers to the water vapor molar concentration, while  $C_3$  represents the remaining inert gas components. At the cathode,

$C_3$  denotes the concentration of  $N_2$ , the major inert component of the humidified air input stream. The hydrogen gas used in fuel cells is often generated by reforming more complex hydrocarbons and so at the anode,  $C_3$  denotes the concentration of  $CO_2$ , the major byproduct of many reforming processes. However, we will eliminate  $C_3$  in favor of the total mixture concentration,  $C = C_1 + C_2 + C_3$ . In fact, it will be convenient to write the mixture evolution equation in terms of the density,  $\rho = \sum_k \rho_k$ , where  $\rho_k = M_k C_k$  and  $M_k$  is the molar mass of the  $k^{th}$  component. The mixture concentration can always be recovered from the density using Eq. (7) below.

The equation of mass conservation for the gas mixture is

$$\frac{\partial \rho}{\partial t} + \nabla \cdot (\rho \mathbf{U}) = 0, \quad (1)$$

where  $\mathbf{U}$  is the mass-averaged mixture velocity. The transport of individual components is affected significantly by inter-species diffusion, and so the conservation laws for the individual components take the following form [3, 16]:

$$\frac{\partial C_k}{\partial t} + \nabla \cdot \underbrace{(C_k \mathbf{U} + \mathbf{J}_k)}_{\mathbf{N}_k} = 0, \quad (2)$$

where  $\mathbf{J}_k$  is the molar diffusive flux (measured relative to the mass-averaged velocity),  $\mathbf{N}_k = C_k \mathbf{U} + \mathbf{J}_k$  is the total (convective plus diffusive) molar flux, and the index  $k = 1$  or  $2$  corresponds to the  $k^{th}$  component in the mixture.

The Maxwell-Stefan equations give the diffusive flux,  $\mathbf{J}_k^*$ , of component  $k$  relative to the *molar-averaged velocity* in terms of the gradients of the component concentrations. The equations take the form:

$$\begin{bmatrix} \mathbf{J}_1^* \\ \mathbf{J}_2^* \end{bmatrix} = -C \mathbb{D} \cdot \begin{bmatrix} \nabla (C_1/C) \\ \nabla (C_2/C) \end{bmatrix}, \quad (3)$$

where the entries of the  $2 \times 2$  diffusivity matrix,  $\mathbb{D} = \begin{bmatrix} D_{11} & D_{12} \\ D_{21} & D_{22} \end{bmatrix}$ , are *Fick diffusivities* that depend on the component concentrations and *binary* gas diffusivities. Details are provided in Appendix I. The fluxes  $\mathbf{J}_k^*$  (relative to the molar-averaged velocity) are related to  $\mathbf{J}_k$  (relative to the *mass-averaged velocity*) via the following equation

$$\begin{bmatrix} \mathbf{J}_1 \\ \mathbf{J}_2 \end{bmatrix} = \mathbb{S} \begin{bmatrix} \mathbf{J}_1^* \\ \mathbf{J}_2^* \end{bmatrix} \quad \text{where} \quad S_{k\ell} = \delta_{k\ell} - \frac{C_k M_\ell}{\rho} \left( 1 - \frac{M_3}{M_\ell} \right) \quad (4)$$

are the entries of the  $2 \times 2$  matrix  $\mathbb{S}$  for  $k, \ell = 1, 2$ , a detail that is overlooked in several other models that use a mass-averaged velocity [3, 21]. Details of this procedure for converting the fluxes can be found in [24].

In an ideal gas mixture, the pressure depends linearly on the mixture concentration (and hence also the density) via the ideal gas law

$$P = CRT, \quad (5)$$

where  $\mathcal{R}$  is the universal gas constant and  $\mathcal{T}$  is the temperature. The final equation needed to close the system is an expression for the mass-averaged velocity of the gas mixture, which is governed by Darcy's law

$$\mathbf{U} = -\frac{K}{\varepsilon\mu}\nabla P, \quad (6)$$

where  $\mu$  is the viscosity of the mixture and the GDL material is characterized by the parameters  $K$  (permeability) and  $\varepsilon$  (porosity). When the material parameters are constant, this equation can be rewritten using the ideal gas law (5) as  $\mathbf{U} = -\Gamma\nabla C$ , where  $\Gamma \doteq \frac{KR\mathcal{T}}{\varepsilon\mu}$ .

Notice that the mixture concentration,  $C$ , can be recovered from the density, component concentrations and molar masses using the formula

$$C = \frac{1}{M_3} \left[ \rho + (M_3 - M_1)C_1 + (M_3 - M_2)C_2 \right]. \quad (7)$$

After substituting for  $\mathbf{U}$  and  $\mathbf{J}_k$  from (3)–(7), the three remaining equations (1)–(2) represent a nonlinear, fully parabolic system of partial differential equations governing the component concentrations  $C_1$  and  $C_2$  and mixture density  $\rho$ .

### 2.3. Boundary Conditions

The boundary of  $\Omega$  consists of segments with four distinct types, labeled I–IV in Fig. 2. We list below the boundary conditions we will apply on each segment for ternary mixtures we consider here. We refer the reader to [20] for a more complete discussion of these boundary conditions in the context of binary mixtures.

- (I) The impermeable boundary at  $y = 0$  between the graphite plate and the GDL where we impose no-flow conditions on the vertical component of the fluxes:

$$J_1^y = 0, \quad (8a)$$

$$J_2^y = 0, \quad (8b)$$

$$N_1^y = 0. \quad (8c)$$

Note that these conditions imply that both  $\mathbf{U} \cdot \hat{\mathbf{n}} = 0$  and  $N_2^y = 0$ .

- (II) The permeable boundary at  $y = 0$ , where we take the mixture concentration (or equivalently, the pressure) immediately inside the GDL to be the same as that in the channel:

$$C = \bar{C}. \quad (9a)$$

That is, the total mixture concentration is uniform throughout the depth of the channel. The other two conditions arise from taking the diffusive flux of each component across the channel/GDL interface to be proportional to the difference in concentrations on either side

$$J_k^y = r_o^k (\bar{C}_k - C_k), \quad (9b)$$

for  $k = 1$  or  $2$ . Here  $\bar{C}_k$  is the depth-averaged component concentration in the channel, and  $r_o^k$  can be interpreted as a *mass transfer coefficient*. An estimate for  $r_o^k$  can be obtained from the

Sherwood number,  $Sh = r_o L/D$ , where  $L$  is a characteristic length. The Sherwood number is typically obtained experimentally and values are available in the literature (see [4] and the references therein).

(III) The permeable boundary at  $y = H$ , between the catalyst and GDL, where

$$J_1^y = r_H C_1. \quad (10a)$$

This is analogous to the condition (9b), where we have assumed the catalytic reaction to be immediate and irreversible so that the reactant concentration inside the catalyst layer is negligible. In practice, the mass transfer coefficient  $r_H$  is tuned so as to match net flux to experimental values, and so is *the only free parameter in this model*. The PEM is impermeable to gases and we take the vertical flux of inert gas to be zero:

$$N_3^y = 0. \quad (10b)$$

The final boundary condition on III arises from a return flux of the end product component (i.e., water vapor) which is proportional to that of the reactant

$$N_2^y = \alpha N_1^y. \quad (10c)$$

The parameter  $\alpha$  is a return coefficient that determines the direction and magnitude of the second-component flux. Since two  $H_2O$  molecules are produced by the reaction for every  $O_2$  molecule consumed, we take  $\alpha = -2$  at the cathode; at the anode on the other hand, no water vapor is produced and so  $\alpha = 0$ .

(IV) The side boundaries at  $x = 0$  and  $x = L$ , where we assume that the solution is periodic in  $x$ .

#### 2.4. Parameter values

The geometrical parameters and gas properties are summarized in Table I. We take identical channel geometry for both electrodes, while the transport coefficients at the boundary differ from the anode to the cathode. The Maxwell-Stefan diffusion coefficients  $\mathfrak{D}_{k\ell}$  are in general temperature-dependent, but in our isothermal model they are taken to be constant and equal to the binary gas diffusivities. The calculation of the Fick diffusivities,  $D_{k\ell}$ , from the Maxwell-Stefan diffusivities is detailed in Appendix I. The humidified gas streams within the flow channels are defined by the mixture concentration  $\bar{C}$  and mole fractions  $\bar{Y}_k = \bar{C}_k/\bar{C}$ . The anode stream contains 60% hydrogen and 30% carbon dioxide, while the cathode consists of 21% oxygen and 69% nitrogen; in both cases, the remaining 10% of the gas is water vapour.

The carbon fiber paper that makes up the GDL belongs to a class of *fibrous porous media*, including such materials as paper, textiles, filters and insulation, that have been thoroughly examined in the materials literature [11]. These fibrous materials are quite distinct from what is more commonly studied in the literature on groundwater flow and reservoir simulations, where the porous media are typically composed of either spheroidal grains (e.g., soil and carbon filters) or cylindrical pores in a solid matrix (e.g., rock). The major distinguishing characteristics of fibrous materials are their anisotropy and porosity, both of which can be quite large in comparison to other porous media. For example, the GDL porosity is approximately  $\varepsilon = 0.74$  whereas for soil and rock, a more typical value is  $\varepsilon = 0.2 - 0.4$ .

Table I. Parameter values (in *cgs* units) used for the GDL model.

Parameter		Values	
$H$	GDL thickness ( <i>cm</i> )	0.05	
$L$	domain width ( <i>cm</i> )	1.0	
$L_c$	channel width ( <i>cm</i> )	0.25	
$L_s$	separation width ( <i>cm</i> )	0.25	
$K$	permeability ( $cm^2$ )	$10^{-8}$	
$\varepsilon$	porosity	0.74	
$\mathcal{R}$	gas constant ( $g\ cm^2/mol\ s^2\ ^\circ K$ )	$8.31451 \times 10^7$	
$\mathcal{T}$	temperature ( $^\circ K$ )	346.15	
$n_x \times n_y$	grid dimensions	$34 \times 24$	
		Anode	Cathode
		( $H_2 / H_2O / CO_2$ )	( $O_2 / H_2O / N_2$ )
$\mu$	viscosity ( $g/cm\ s$ )	$2.01 \times 10^{-4}$	$2.24 \times 10^{-4}$
$\Gamma = \frac{K\mathcal{R}\mathcal{T}}{\varepsilon\mu}$	convection parameter ( $cm^5/s\ mol$ )	$1.94 \times 10^6$	$1.74 \times 10^6$
$\mathcal{D}_{kl}$	Maxwell-Stefan diffusivities ( $cm^2/s$ )		
	$k, \ell = 1, 2$	0.457	0.124
	1, 3	0.316	0.104
	2, 3	0.089	0.123
$M_k$	molar masses ( $g/mol$ )	2.0 / 18.0 / 44.0	32.0 / 18.0 / 28.0
$\bar{Y}_k = \bar{C}_k / \bar{C}$	channel mole fractions	0.60 / 0.10 / 0.30	0.21 / 0.10 / 0.69
$\bar{C}$	channel concentration ( $mol/cm^3$ )	$3.475 \times 10^{-5}$	$3.475 \times 10^{-5}$
$\bar{\rho} = \sum_k M_k \bar{C}_k$	channel density ( $g/cm^3$ )	$5.629 \times 10^{-4}$	$9.673 \times 10^{-4}$
$r_o^k$	bottom transfer rates ( $cm/s$ )	10.0	10.0
$r_H$	top transfer rate ( $cm/s$ )	0.2	0.8
$\alpha$	return coefficient	0.0	-2.0

A larger porosity also translates into a larger permeability. Typical values reported in experiments are summarized in Table II.

Because the fibers making up the GDL are oriented so that their axes lie primarily in the plane of the paper, the material is anisotropic and hence the transport coefficients are different in the through-plane and in-plane directions. The permeability and diffusivity are tensor quantities, which can be taken to be diagonal [11]:  $\mathbb{K} = \text{diag}(K^x, K^y)$  and  $\mathbb{D}_{kl} = \text{diag}(D_{kl}^x, D_{kl}^y)$ . Alternatively, these coefficients can be rewritten in the form  $\mathbb{K} = K \text{diag}(\chi_K, 1)$  and  $\mathbb{D}_{kl} = D_{kl} \text{diag}(\chi_D, 1)$ , where the through-plane transport coefficients serve as reference values, and  $\chi_K = K^x/K^y$  and  $\chi_D = D_{kl}^x/D_{kl}^y$  are *anisotropy ratios*. Since flow along the axis of the fibers is less hindered than that across fiber cross-sections, the in-plane coefficients are significantly greater than their through-plane counterparts, so that both  $\chi_K$  and  $\chi_D$  are greater than one in magnitude.

Perhaps the most important aspect of the GDL, which sets it apart from most other porous media, is

the very small spatial dimensions under consideration, since the thickness of the GDL is 0.05 *cm* or less. Typical distances in other porous media, particularly groundwater transport, are on the order of tens or hundreds of centimeters; this disparity in length scales can lead to very significant differences in solution behavior. A clear measure of the quantitative difference between various flows is the Péclet number,  $Pe = \Gamma \bar{C}/D$ , which is the ratio of convective to diffusive components of mass transport. For the typical parameter values listed in Table II,  $Pe$  is four orders of magnitude larger for gas flow in the GDL than for that in soil and rock. Another interpretation of the Péclet number is as a ratio of time scales corresponding to convection and diffusion, and these are also listed in the Table for comparison purposes.

Table II. Comparison of porous media parameters for carbon fiber paper and sand/soil/rock (sources: [9, 10, 17, 23, 26, 28]).

	<b>GDL</b>	<b>Soil/rock</b>
Porosity ( $\varepsilon$ )	0.70–0.80	0.10–0.40
Permeability ( $K$ , $cm^2$ )	$10^{-7}$ – $10^{-9}$	$10^{-7}$ – $10^{-13}$
Length scale ( $H$ , $cm$ )	0.05	$10^1$ – $10^3$
Péclet number ( $Pe = \Gamma \bar{C}/D$ )	$3 \times 10^3$	$3 \times 10^{-1}$
Derived time scales:		
convective ( $H^2/\Gamma \bar{C}$ )	$3 \times 10^{-6}$	$3 \times 10^4$
diffusive ( $H^2/D$ )	$9 \times 10^{-3}$	$9 \times 10^3$

### 3. The Finite Volume Method

#### 3.1. Spatial discretization

We have chosen to employ a spatial discretization based on finite volumes (also known as control volumes), an approach which is very commonly used for problems involving conservation laws [19]. For this method, the conservation properties of the original equations are passed along to their discrete analogues. The importance of conservative schemes has already been recognized for the simulation of mass transport in fuel cells and other related problems (e.g., [3, 8, 23]).

Our rectangular domain is divided into a regular,  $n_x \times n_y$  grid as pictured in Figure 3. Density and concentration unknowns are defined as averages over each cell, and located at cell centers. The flux and velocity unknowns, on the other hand, are defined as edge averages, and are located at the center of each cell edge (see Figure 3). The grid spacings  $\Delta x = L/n_x$  and  $\Delta y = H/n_y$  are taken to be constant in both directions. We use a method-of-lines approach and discretize first in the spatial variables so that the unknown solution components remain continuous functions of time. The semi-discrete unknowns at cell centers are identified by

$$\rho_{i,j}(t), C_{k;i,j}(t), \quad \text{for } i = 1, \dots, n_x, \quad j = 1, \dots, n_y, \quad \text{and } k = 1, 2,$$

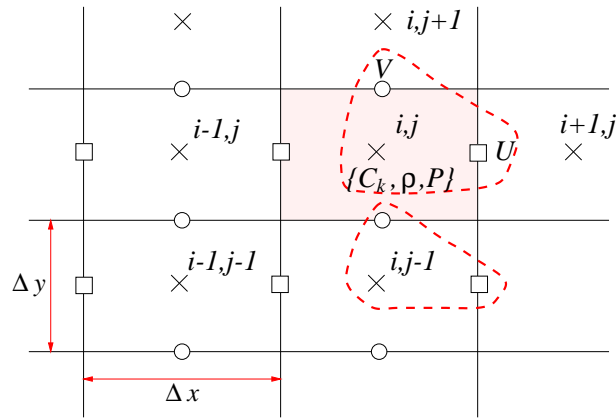


Figure 3. A picture of the grid used to discretize the problem, with the placement of unknowns indicated in a cell: “x” for  $P$ ,  $\rho$  and  $C_k$ ; “o” for  $V$  and  $J^y$ ; and “□” for  $U$  and  $J^x$ . The dashed line encloses those points which are labeled with the subscript  $i, j$ .

at horizontal cell edges by

$$U_{i,j}(t), J_{k;i,j}^x(t) \quad \text{for } i = 0, \dots, n_x, \quad j = 1, \dots, n_y, \quad \text{and } k = 1, 2,$$

and at vertical cell edges by

$$V_{i,j}(t), J_{k;i,j}^y(t) \quad \text{for } i = 1, \dots, n_x, \quad j = 0, \dots, n_y \quad \text{and } k = 1, 2.$$

The discrete versions of (1)–(5) are obtained by integrating the equations over each cell  $i, j$  to obtain

$$\frac{d\rho_{i,j}}{dt} + \frac{1}{\Delta x} (\hat{\rho}_{i,j}^\square U_{i,j} - \hat{\rho}_{i-1,j}^\square U_{i-1,j}) + \frac{1}{\Delta y} (\hat{\rho}_{i,j}^\circ V_{i,j} - \hat{\rho}_{i,j-1}^\circ V_{i,j-1}) = 0, \tag{11a}$$

$$\begin{aligned} \frac{dC_{k;i,j}}{dt} + \frac{1}{\Delta x} (\hat{C}_{k;i,j}^\square U_{i,j} - \hat{C}_{k;i-1,j}^\square U_{i-1,j} + J_{k;i,j}^x - J_{k;i-1,j}^x) \\ + \frac{1}{\Delta y} (\hat{C}_{k;i,j}^\circ V_{i,j} - \hat{C}_{k;i,j-1}^\circ V_{i,j-1} + J_{k;i,j}^y - J_{k;i,j-1}^y) = 0, \end{aligned} \tag{11b}$$

$$J_{k;i,j}^x = -\frac{S_{k,1}^x D_{k,1}^x}{\Delta x} \hat{C}_{i,j}^\square \left( \frac{C_{1;i+1,j}}{C_{i+1,j}} - \frac{C_{1;i,j}}{C_{i,j}} \right) - \frac{S_{k,2}^x D_{k,2}^x}{\Delta x} \hat{C}_{i,j}^\square \left( \frac{C_{2;i+1,j}}{C_{i+1,j}} - \frac{C_{2;i,j}}{C_{i,j}} \right), \tag{11c}$$

$$J_{k;i,j}^y = -\frac{S_{k,1}^y D_{k,1}^y}{\Delta y} \hat{C}_{i,j}^\circ \left( \frac{C_{1;i,j+1}}{C_{i,j+1}} - \frac{C_{1;i,j}}{C_{i,j}} \right) - \frac{S_{k,2}^y D_{k,2}^y}{\Delta y} \hat{C}_{i,j}^\circ \left( \frac{C_{2;i,j+1}}{C_{i,j+1}} - \frac{C_{2;i,j}}{C_{i,j}} \right), \tag{11d}$$

$$U_{i,j} = -\frac{\chi_k \Gamma}{\Delta x} (C_{i+1,j} - C_{i,j}), \tag{11e}$$

$$V_{i,j} = -\frac{\Gamma}{\Delta y} (C_{i,j+1} - C_{i,j}). \tag{11f}$$

For the velocity calculations in Eqs. (11e) and (11f), the mixture concentration  $C_{i,j}$  is obtained from  $C_{k;i,j}$  and  $\rho_{i,j}$  using Eq. (7).

We will assume for the present that porosity, viscosity, permeability, and diffusivities are constant. However, the method can easily be generalized to the case where the material parameters and transport coefficients depend on position, or the solution itself.

For a cell-centered quantity  $q_{i,j}$  (where  $q = C$  or  $\rho$ ),  $\hat{q}_{i,j}$  denotes an averaged value located at a cell edge. The superscript “ $\square$ ” or “ $\circ$ ” denotes whether the average value is located on a vertical edge or a horizontal edge respectively (refer to Fig. 3). For example, the density on vertical edges (labelled “ $\square$ ”) is given by the second-order average  $\hat{\rho}_{i,j}^{\square} = \frac{1}{2}(\rho_{i,j} + \rho_{i+1,j})$ . The expressions for  $\hat{\rho}^{\circ}$ ,  $\hat{C}_k^{\square}$ ,  $\hat{C}_k^{\circ}$ , and  $\hat{C}^{\circ}$  are defined in a similar manner.

3.2. Discrete boundary conditions

The discrete periodic conditions along the vertical boundaries,  $x = 0$  and  $x = L$ , are very straightforward to implement. The difference formulas in Eqs. (11), when evaluated at cells adjacent to the top and bottom boundaries, involve points that lie outside the physical domain. In order to remedy this situation, we define a horizontal row of “ghost cells” on each edge of the domain (see Figure 4) inside which are defined ghost values  $\rho_{i,0}$  and  $\rho_{i,n_y+1}$  (and similarly for  $C_k$ ). The discrete versions of the boundary conditions can then be written without difficulty using our staggered finite volume grid, thereby allowing the solution values located in ghost cells to be determined in terms of interior solution values. As a result, the discrete boundary conditions on the top and bottom of the domain represent a

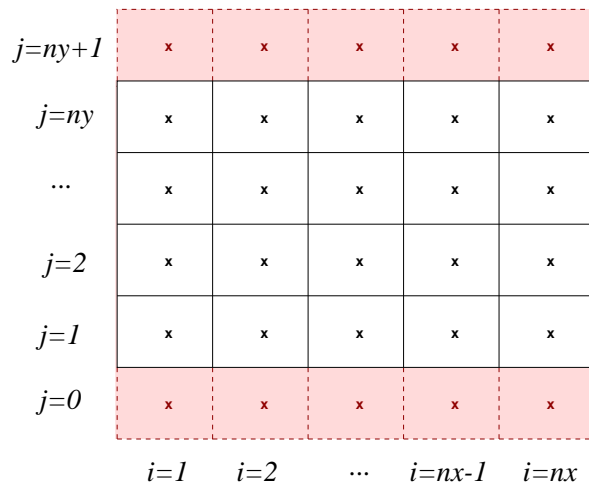


Figure 4. A diagram showing the relationship between the actual grid and the ghost cells introduced for satisfying discrete boundary conditions.

total of  $2 n_x$  systems of non-linear algebraic equations. The system arising at each boundary point consists of 3 coupled equations to be solved for the unknown ghost values in that cell. We employ a nonlinear solver to solve each of these systems, which we describe in more detail in the next section.

### 3.3. Time discretization and stiffness

The semi-discrete equations (11) represent a system of  $3n_x n_y$  ODEs for the unknown functions  $\rho_{i,j}(t)$ ,  $C_{1;i,j}(t)$ , and  $C_{2;i,j}(t)$ . In order to solve this system numerically, we need to discretize the equations in time. Our approach will be to start with some initial distribution of the concentrations, and then step the solution to steady state.

The most straightforward method would be to replace the time derivatives with a forward difference approximation, thereby obtaining a fully explicit method. Unfortunately, this simple approach is impractical, because it requires an extremely small time step for the numerical solution to remain stable. This severe restriction on time step can be explained using the well-known stability criterion for a centered, second order, explicit discretization of the convection–diffusion equation (see [23], for example). In our porous flow model, the convective terms in the equations actually take a similar form to the diffusive terms, involving second derivatives of the solution. Therefore, when we linearize the equations of motion and apply the standard stability condition for centered schemes, we find that the time step restriction reduces to

$$\Delta t \leq \min \left( \frac{1}{D}, \frac{1}{\Gamma C}, \frac{1}{\Gamma C \bar{Y}_k} \right) \left( \frac{2}{(\Delta x)^2} + \frac{2}{(\Delta y)^2} \right)^{-1},$$

which encompasses restrictions from both diffusion ( $\frac{1}{D}$ ) and convection ( $\frac{1}{\Gamma C}$ ). For a typical choice of parameters listed in Table I, this translates into the condition  $\Delta t \lesssim 2 \times 10^{-5}$  for the diffusion terms and  $\Delta t \lesssim 3 \times 10^{-9}$  for the convective terms. If one considers that a steady state solution is typically reached by time  $t = 0.5$  s, it is clear that a total of  $10^8 - 10^9$  equally-spaced time steps are required for this simple explicit computation to remain stable.

From Table II and the stability analysis above, it is clear that the system possesses two disparate time scales. In the paper [20], the effect of these two time scales on the solution behavior was analysed in detail. We showed that initially the total mixture concentration (or equivalently the pressure) relaxes to a quasi-steady state on the convective time scale. On the slower diffusive scale, flow velocities are relatively small and diffusive effects generate gradients in mole fractions which in turn adiabatically drive the mixture concentration along a family of quasi-steady states to the final steady solution. For computations employing explicit time stepping, it is this convergence of the mixture concentration onto the manifold of quasi-steady states that forces the time step to be so small.

Our model equations therefore comprise a stiff system for which an explicit time discretization is inappropriate, and hence an implicit method with some form of variable time-step selection must be used. Because the equations and boundary conditions are highly non-linear, our approach was to use an existing numerical solver for integrating non-linear systems of ODEs, namely DASSL [18], which uses the backward differentiation formulas of orders 1 through 5. This code is designed to solve general differential–algebraic systems of the form  $G(t, y, dy/dt) = 0$  using a time step selection strategy that controls the error relative to user-specified error tolerances. We used the built-in finite difference approximation to the Jacobian matrix, took advantage of the banded structure of the Jacobian, and used absolute and relative error tolerances of  $\text{RTOL} = \text{ATOL} = 1e-6$ .

Another potential advantage to using DASSL is its very general framework that allows the time-independent discrete boundary conditions to be included as algebraic constraints, which can then be

solved simultaneously with the differential equations. However, all of our attempts to use DASSL to solve both the equations and boundary conditions resulted in very poor convergence, perhaps due to scaling problems with the boundary conditions. As a result, we have instead solved the boundary conditions separately within each iteration using the non-linear solver DNSQ (which is a modification of Powell's hybrid method, implemented in the SLATEC library [22]). The convergence using this approach is quite rapid, requiring on average only about 5 function evaluations per call to DNSQ. In practice, a steady-state computation on a  $34 \times 24$  grid requires on the order of 1000 residual evaluations and half that number of Jacobian calculations. This translates into approximately 1–2 minutes of CPU time on a Dell Precision Workstation (733 MHz Pentium III processor, 256 Mb RAM, with a SPEC CFP2000 benchmark rating of 242, see <http://www.spec.org/osg/cpu2000/results/>).

#### 4. Numerical Results

##### 4.1. Convergence study

In order to verify that our numerical scheme is second order accurate in space, we performed a convergence study using computations on a sequence of grids of size  $16 \times 12$ ,  $32 \times 24$ ,  $64 \times 48$  and  $128 \times 96$ . The physical parameters were chosen to correspond to the cathode in Table I, and the solution was computed up to time 5.0 *sec*. We based our error measure on the reactant mole fraction, and computed differences between the solution values on successive grids. Let  $Y^{(m-1)}$  and  $Y^{(m)}$  denote the solutions on grid level  $m - 1$  and the next finer grid  $m$  with twice as many points in both coordinate directions (where  $Y^{(1)}$  is computed on the  $16 \times 12$  grid). If the difference between solutions on successive grids is given as  $E^{(m)} = \|Y^{(m)} - Y^{(m-1)}\|_p$  (in the discrete  $p$ -norm) then the rate of convergence is approximated by

$$R^{(m)} \approx \log_2 \left( \frac{E^{(m-1)}}{E^{(m)}} \right).$$

In Table III we summarize the successive differences and convergence rates for two choices of norm (the max-norm and discrete 2-norm) and the rate in both cases approaches the expected value of 2.

Table III. Convergence rates for cathode calculations on a sequence of refined grids.

$m$	$n_x \times n_y$	Max-norm		2-norm	
		$E_\infty^{(m)}$	$R^{(m)}$	$E_2^{(m)}$	$R^{(m)}$
1	$16 \times 12$	—	—	—	—
2	$32 \times 24$	$3.45 \times 10^{-4}$	—	$1.16 \times 10^{-3}$	—
3	$64 \times 48$	$8.83 \times 10^{-5}$	1.97	$2.91 \times 10^{-4}$	1.99
4	$128 \times 96$	$2.14 \times 10^{-5}$	2.05	$7.32 \times 10^{-5}$	2.01

#### 4.2. Base case

As our base case we take isotropic transport coefficients (i.e.,  $\chi_D = \chi_K = 1$ ) and zero pressure difference between adjacent channels. We focus for the present on the cathode, and use the gas mixtures and transport parameters listed in Table I. Under the assumption that all of the reactant gas which reaches the catalyst layer is immediately consumed, the reactant flux is proportional to the current density in the cell. We use the vertical component of the total reactant flux at the top boundary,  $N_1^y|_{y=H}$ , as a performance indicator, since this quantity is related to the current produced by the cell. We take the membrane transport coefficient  $r_H$  so that the computed solution has a current density of  $1.0 \text{ A/cm}^2$  for our base case, but then keep  $r_H$  fixed for comparative runs.

Fig. 5 depicts a surface plot of the reactant mole fraction  $Y_1$  alongside the profile of reactant flux,  $N_1^y|_{y=H}$ . It is evident that in the absence of pressure gradients, the solution is symmetric about the centerline  $x = L/2$ . The mole fraction plot shows that the  $O_2$  gas concentration decreases from channel to membrane as the reactant is consumed. There are two very well-defined peaks in the reactant flux immediately above the channels which indicate thus regions of enhanced reaction. The variation in flux across the membrane is quite significant, which may indicate that those portions of the catalyst lying above the landing area are underutilized. The flux computed using the two-component (Fickian)

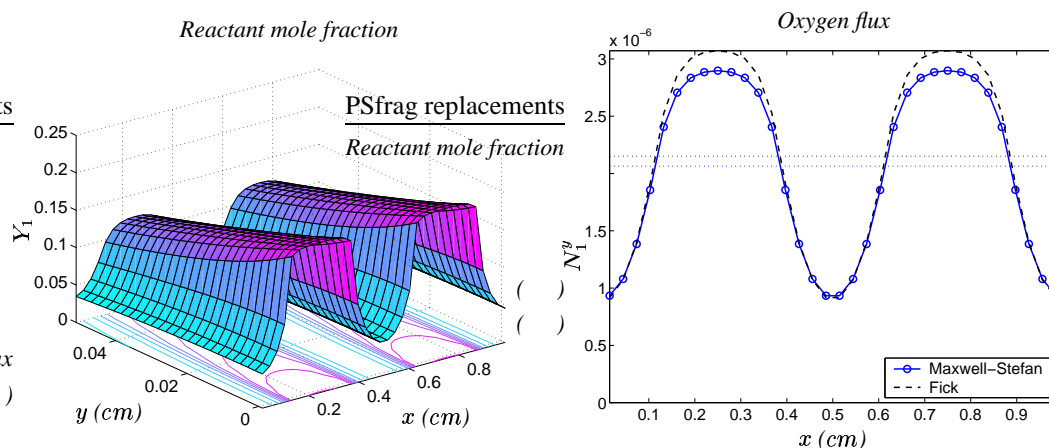


Figure 5. Reactant mole fraction (left) and total reactant flux at the membrane (right) for the cathode “base case.”

model is included for comparison. Here, the water vapour and nitrogen are lumped together into a single component with appropriately-averaged molar mass. The two-component model overestimates the average flux by not including the additional “interspecies friction” present in the three-component case.

The flow of the gas mixture and reactant are evident in the vector plots of velocity  $\mathbf{U}$  and reactant flux  $\mathbf{N}_1$  in Fig. 6. The return flux of water vapor generated at the catalyst layer is clearly indicated in the velocity plot, where partial pressure gradients due to the water vapor cause a net downward flux of vapor. However, the velocity remains small in comparison to the diffusive flux at steady state, resulting in a net reactant flux that is directed vertically upwards throughout the domain.

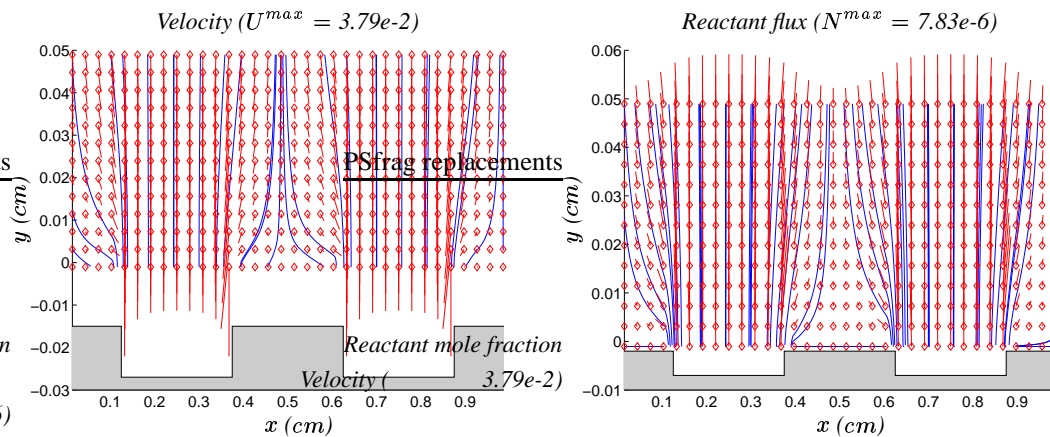


Figure 6. Vector plots of velocity and total flux for the cathode “base case.” The velocity and flux streamlines are superimposed on the vector plots to highlight the flow direction. The locations of the flow channels and landing areas are indicated by the shaded regions.

#### 4.3. Transient calculations and stiffness

The solution plots in Fig. 7 demonstrate the dominance of convection over very short time scales and the role of diffusion in the subsequent convergence to steady state. In this figure, point values of the mixture concentration  $C$  and oxygen mole fraction  $Y_1$  (evaluated at mid-channel, just inside the lower boundary) are plotted against time on a log scale. The initial convection-dominated flow drives the upswing in the  $C$  curve near  $t = 10^{-5}$  s, since gradients in mixture concentration (or equivalently pressure) give rise to the gas velocity. The mole fraction, on the other hand, remains virtually constant until  $t = 10^{-3}$  sec, at which time the diffusive effects take hold and lead to much slower variations in both  $C$  and  $Y_1$ .

The time step corresponding to the same computation is displayed in the plot on the right of Fig. 7. The  $\Delta t$  chosen by DASSL is initially required to be very small (less than  $10^{-9}$ ) but then increases linearly with time on a log-log scale. During the diffusive transient (between times  $10^{-3}$  and  $10^{-1}$ ), all solution components experience significant variation; consequently, the time step during this interval remains nearly constant as evidenced by the clustering of points on the  $\Delta t$  plot. We conclude that the adaptive time step selection procedure is very effective at resolving changes in the solution on the widely-varying convective and diffusive time scales, relaxing the time step restriction at later times once the solution has reached steady state.

#### 4.4. Pressure differences between channels

Flow channels in a Ballard fuel cell typically follow a serpentine path that doubles back and forth across the graphite plate. There is a continuous drop in the gas pressure along the length of each flow channel; as a result, a pressure difference between adjacent channels of  $\Delta P = 10^4$  dyne/cm<sup>2</sup> is not uncommon. In fact, Yi and Nguyen [28] report that even for relatively small pressure drops of 2.5% or

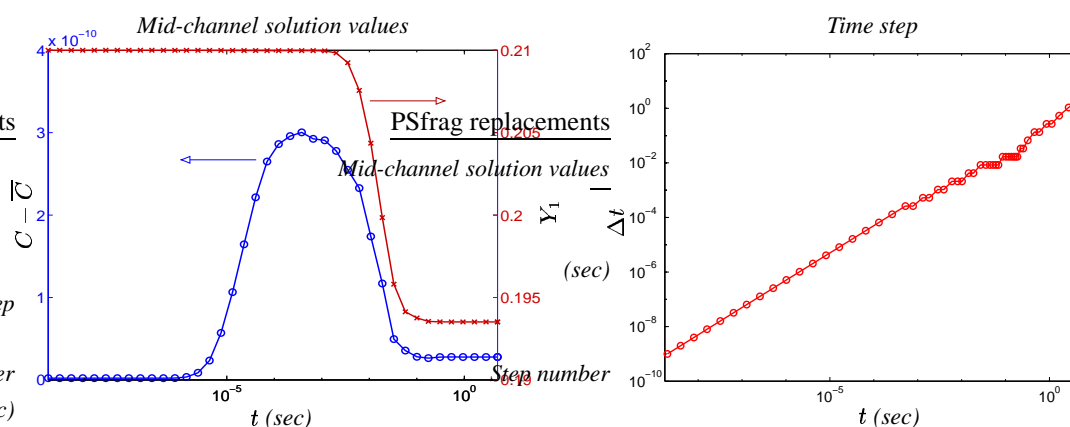


Figure 7. Plots of mid-channel point values of  $C$  and  $Y_1$  (on the left) and time step (on the right).

less (at an operating pressure of  $10^6$  *dyne/cm*<sup>2</sup>), fuel cells with interdigitated flow fields exhibited a performance improvement of between 60 and 100%.

Due to the dominance of convection, even a small pressure difference introduced between adjacent flow channels breaks the symmetry of the solution and alters flow behavior significantly. Fig. 8 shows two plots of the computed oxygen flux for corresponding to  $\Delta P = 1 \times 10^4$  and  $4 \times 10^4$  *dyne/cm*<sup>2</sup> (i.e.,  $\Delta P/P = 0.01$  and 0.04). There is a very clear right-to-left cross-flow of oxygen, and although some of the reactant exits the domain through the corners of the left channel, the overall flux of oxygen remains directed upward through the center of the left channel. This is consistent with the numerical results obtained in [28] for a 2D steady-state model of mass transport in PEM fuel cells.

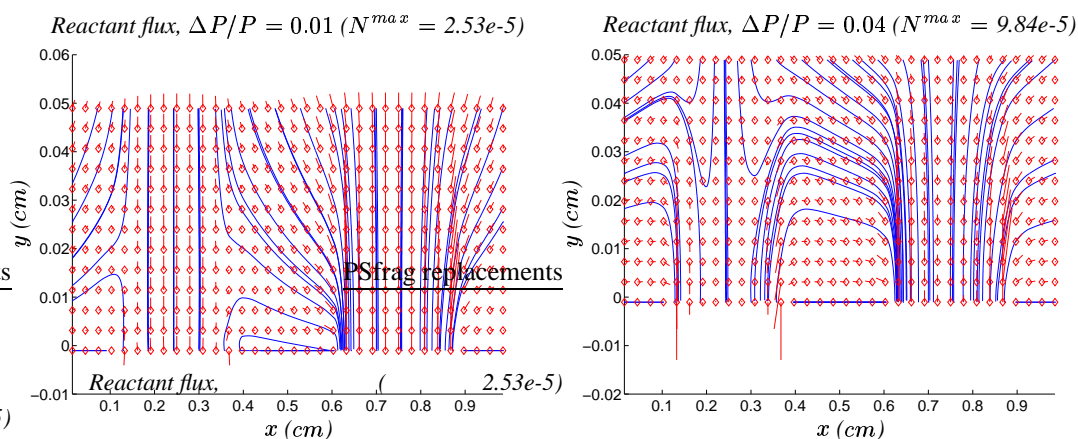


Figure 8. Vector plots of the total flux for two values of the channel pressure drop.

Changes in the flux profile at the catalyst layer as a result of these pressure differences are illustrated

in Fig. 9. While the cross-flow engendered by pressure differences appears from the vector plots to

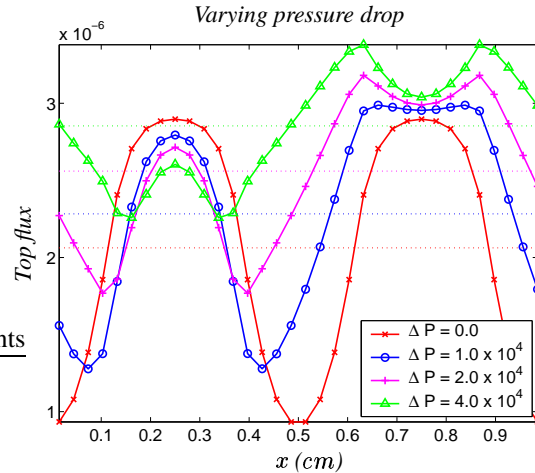


Figure 9. Comparison of membrane reactant flux for four different values of the channel pressure drop ( $\Delta P/P = 0.0, 0.01, 0.02,$  and  $0.04$ ). The average flux corresponding to each curve is plotted as a dotted line.

direct reactant away from the upper boundary, the opposite is true. In fact, the enhanced transport due to cross-flow actually increases the reactant flux. If we take the average flux at the top boundary as a measure of performance, then pressure differences clearly have the beneficial impact of levelling out the peaks in the profiles, while also increasing the transport of reactant gas to the catalyst.

Fig. 10 demonstrates the relationship between the horizontal cross-flux and membrane flux as the pressure difference between channels is increased. The curve marked with “o” denotes the average of the vertical reactant flux component across the top boundary, while the second curve gives the ratio between this averaged top flux and the average value of the horizontal flux along the centerline (i.e.,  $N_1^x|_{x=L/2}$ ). As the channel pressure drop is increased, the horizontal reactant flow clearly begins to dominate the vertical flux component. However, the reactant flux at the membrane-catalyst interface is not adversely affected by the cross-flow.

#### 4.5. Anisotropy and inhomogeneity in the GDL

Fibrous porous materials have been studied in considerable detail both experimentally [14] and theoretically (for regular arrays of cylindrical fibers [11]). These works have shown that in materials such as the GDL, the permeability tensor is anisotropic and has components in the in-plane and through-plane directions that differ by up to a factor of 20, or  $1 \leq \chi_\kappa \leq 20$  in our notation.

Much less attention has been paid to the effect of anisotropy on the diffusivity of a gas in porous media. We appeal to the work of Koch & Brady [12] who derive expressions for the various directional diffusivities in fibrous beds of the form  $\chi_D = (1 - \varepsilon + \varepsilon^2)/(1 - 2\varepsilon + 2\varepsilon^2)$ , where  $\varepsilon$  denotes the void fraction. Consequently, their anisotropy ratio for diffusivity satisfies  $1 \leq \chi_D \leq \frac{3}{2}$ , with the maximum value occurring at  $\varepsilon = \frac{1}{2}$ . However, Chernyakov [6] uses an alternate derivation that yields

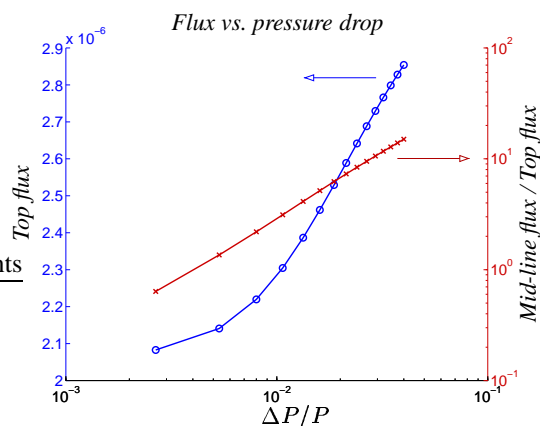


Figure 10. Variations in the membrane reactant flux and the midline-to-top flux ratio versus pressure drop.

significantly larger values of the anisotropy ratio, and so for this work we have chosen values lying in the range  $1 \leq \chi_D \leq 4$ .

We performed several simulations in which the through-plane permeability and diffusivities ( $K^y$  and  $D_{k\ell}^y$ ) were fixed, while the in-plane coefficients were varied. On the left of Fig. 11 are shown several plots of the membrane reactant flux as  $\chi_D$  is increased from 1 to 4 and  $\chi_K$  is held at 1. Increasing the in-plane diffusivity clearly evens out the flux profile while at the same time increasing the average membrane flux and enhancing performance.

On the right of Fig. 11 are a similar set of plots with a pressure difference between the two channels of  $\Delta P/P = 0.001$ . Comparing to the results from Section 4.4, where there was almost no change in flux profiles from the base case using this relatively small value  $\Delta P$ , it is evident that the anisotropy of the GDL may have even more impact on situations where there is cross-flow. To investigate the effect of anisotropy in the permeability, we have included in Fig. 11 the results of simulations with  $\chi_K = 1$  and 10 (with  $\chi_D = 4$  fixed). While there is some change in the flux profiles, the sensitivity to permeability is much less pronounced, pointing to the clear dominance of diffusion over convection at steady state in the parameter regime under which fuel cells operate.

Another source of non-uniformity in the GDL is the spatial variation in porous structure that arises due to compression of the electrode above the solid landing areas. The graphite plates on either side of the MEA are bolted together under significant pressure that helps to seal the fuel cell assembly against gas leaks. Compression is known to significantly alter the porous structure of the electrode, thereby affecting fuel cell performance [15]. We are able to capture this effect by allowing the porosity to vary as a function of  $x$ . Using a composition of functions of the form  $\sin^{2n}(x)$  that are appropriately scaled and translated, we have constructed a function (plotted in Fig. 12) which has the effect of varying the porosity continuously between values of  $\varepsilon_{min}$  (over each landing area) and  $\varepsilon_{max}$  (over the channels).

In this next set of simulations, we take the transport coefficients to be isotropic, and let the porosity vary in space as just described. In isotropic porous media, the dependence of the diffusion coefficient on porosity is often approximated using the empirical formula  $D^{eff} = \varepsilon^{1.5} D^{gas}$  (attributed

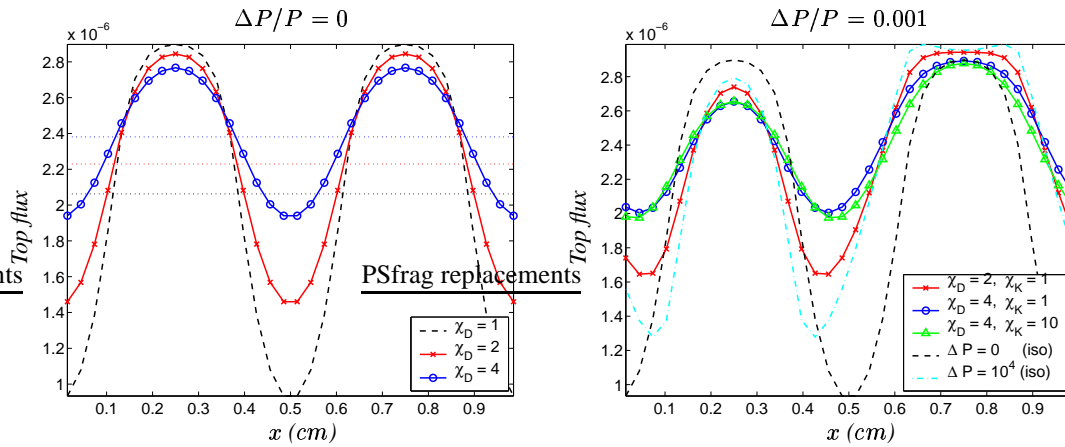


Figure 11. Variation in the membrane reactant flux for various levels of anisotropy in the transport coefficients. The results in the left figure are for a zero channel pressure difference. The right figure corresponds to  $\Delta P/P = 0.001$  which, while nonzero, is still small in comparison with the simulations in Sec. 4.4. The isotropic results for  $\Delta P/P = 0$  and 0.01 are shown as dotted lines for comparison.

to Bruggeman [1]), which relates the effective diffusivity in the porous medium to that of a free gas. While this approximation is strictly valid only for porous media consisting of spherical grains, we apply it in the current isotropic situation to illuminate the possible effects of a spatially-varying porosity. The

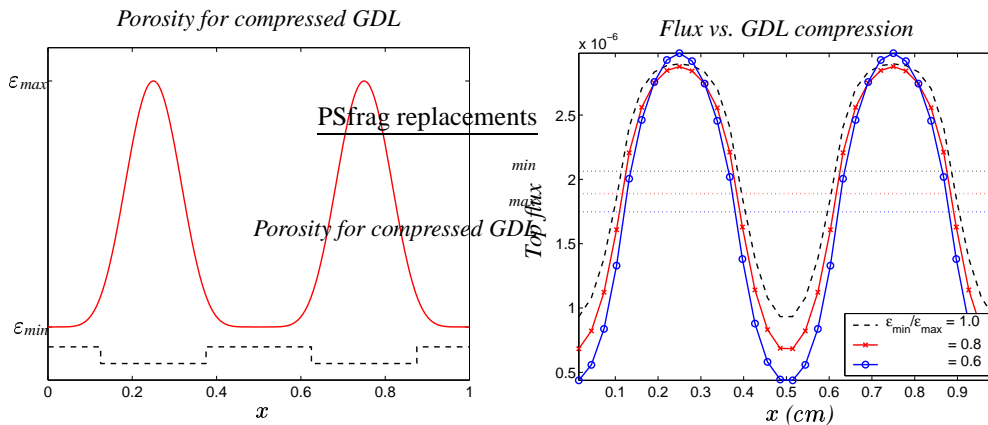


Figure 12. Variable porosity simulations use a porosity that varies in the  $x$ -direction as pictured on the left, with the channels shown for comparison. The flux profiles corresponding to porosity ratios of  $\varepsilon_{min}/\varepsilon_{max} = 1.0, 0.8$  and  $0.6$  are shown in the plot on the right.

right hand plot in Fig. 12 compares the computed reactant flux profiles for several values of the ratio  $\varepsilon_{min}/\varepsilon_{max}$  with  $\varepsilon_{max}$  fixed at 0.74. Compressing the GDL reduces the porosity (and hence also the

diffusion coefficients) over the landing area, which in turn decreases the overall flux of reactant to the catalyst layer, particularly above the landing areas. Compression has a detrimental impact on fuel cell performance, leading to increased variation of reactant flux.

#### 4.6. Comparison of anode and cathode

The reactant flux in the anode is much less of a limiting factor in fuel cell performance due in part to the large diffusivity of hydrogen gas in comparison with oxygen. We choose a base case for the anode by selecting the membrane mass transport coefficient  $r_H = 0.2$  to yield a steady state current density of  $1.0 \text{ amp/cm}^2$ . The resulting membrane flux profile pictured in Fig. 13 (for  $\Delta P = 0$ ) shows the characteristic peaks above the channels. However, the variation in flux is 20% compared with 200% for the cathode (see Fig. 5). The reactant gas is thus much more evenly distributed across the anode catalyst layer, which is desirable in terms of optimizing performance.

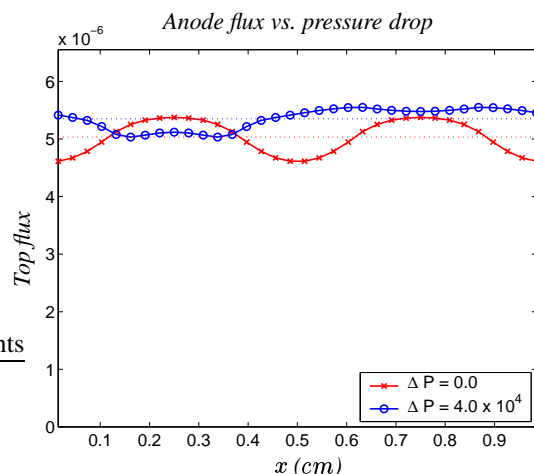


Figure 13. Reactant mole fraction (left) and total reactant flux at the membrane (right) for the anode.

The anode is also much less sensitive to pressure differences between successive channels, as illustrated by the curve labelled  $\Delta P = 4 \times 10^4$  in Fig. 13. The effect of a nonzero pressure difference is similar, in that peaks and valleys in the flux profile are smoothed out, and the average flux is increased. However, the relative changes for the anode are much smaller than for the cathode.

## 5. Conclusions

The gas diffusion layer is an essential component of the proton exchange membrane fuel cell, and limitations due to mass transport in the GDL are known to be significant. However, most of the models appearing in the fuel cell literature have focused on the complex coupling between heat, mass, and charge transport between other components of the fuel cell, and in the process have simplified aspects

of the GDL by ignoring convection or assuming mass transport coefficients are constant and isotropic.

In this work, we have presented a model of mass transport in the GDL which includes as much detail as possible of the physics and material properties. The interspecies diffusion is governed by the Maxwell-Stefan equations, while convection in the porous layer is modeled by Darcy's law. The resulting system of nonlinear diffusion equations is solved using a finite volume spatial discretization in combination with implicit backward differentiation formulas in time. Because of the nonlinear coupling introduced through the boundary conditions, a careful discretization of the boundary conditions is necessary in order to maintain second order accuracy throughout the entire computational domain. Numerical experiments confirm that the discretization is second order accurate in space and that the implicit time-stepping algorithm solves this stiff problem efficiently.

Our numerical simulations demonstrate that material properties of the fibrous GDL such as anisotropy and spatial inhomogeneities due to stack compression can have a significant influence on the reactant gas transport, and hence also on fuel cell performance. Small pressure differences between neighboring channels can also influence performance by generating through-plane cross-flow that may locally increase performance by facilitating reactant transport to the catalyst layer and improving catalyst utilization.

The originality of this work derives not only from our mathematical model, but also from its use of the numerical solution algorithm and the engineering conclusions we draw from it. On the modelling side, we have focused on correctly incorporating the Maxwell-Stefan equations for multicomponent diffusion and deriving consistent boundary conditions. In this respect, our work differs significantly from other related fuel cell models that have appeared in the literature. Secondly, we have taken a very careful approach to discretizing the system, and particularly the nonlinear boundary conditions, so that the resulting numerical method is fully second order accurate in space. Finally, we investigated the sensitivity of reactant transport to GDL anisotropy and cross-channel pressure differences which have received little or no attention in the fuel cell literature.

The mass transport model we have presented is an ideal formulation to begin addressing other aspects of the physics, such as heat and water transport, which we expect will also be affected significantly by the anisotropy and inhomogeneity in the GDL material. In the future, we will including these added effects in a more complete fuel cell model that should improve on the predictive property of mathematical models in the fuel cell community. We also plan to extend the model to a three-dimensional geometry, taking into account variations along-the-channel, which will require more efficient numerical solution procedures and particularly the development of effective preconditioning strategies.

## APPENDIX

## I. Multicomponent Maxwell–Stefan Model

The Maxwell–Stefan equations for the general case of  $n_c \geq 2$  components take the form [24]

$$-\nabla \left( \frac{C_k}{C} \right) = \sum_{\substack{\ell=1 \\ \ell \neq k}}^{n_c} \frac{C_\ell \mathbf{J}_k^* - C_k \mathbf{J}_\ell^*}{C^2 \mathfrak{D}_{k\ell}}. \quad (12)$$

The *Maxwell–Stefan diffusion coefficients*, denoted  $\mathfrak{D}_{k\ell}$ , are determined from the mixture mole fractions and the *binary diffusion coefficients*, reported in chemical tables for mixtures consisting of only two gases. Equation (12) represents a system of  $(n_c - 1)$  equations that can be inverted to obtain the fluxes in terms of concentration gradients

$$[\mathbf{J}_k^*] = -C \mathbb{D} \cdot \left[ \nabla \left( \frac{C_k}{C} \right) \right], \quad (13)$$

where  $[\mathbf{J}_k^*] = \begin{bmatrix} \mathbf{J}_1^* \\ \mathbf{J}_2^* \end{bmatrix}$  and  $\mathbb{D} = (D_{k\ell})$  is an  $(n_c - 1) \times (n_c - 1)$  matrix.

The *Fick diffusivities*,  $D_{k\ell}$ , are in general composition-dependent, and come from inverting (12), along with the identity  $\sum_{k=1}^{n_c} \mathbf{J}_k^* = 0$ . In the case of a ternary gas ( $n_c = 3$ ), the Fick diffusivities are given by the following [24, p. 80]:

$$\begin{aligned} D_{11} &= \mathfrak{D}_{13}(Y_1 \mathfrak{D}_{23} + (1 - Y_1) \mathfrak{D}_{12})/S, \\ D_{12} &= Y_1 \mathfrak{D}_{23}(\mathfrak{D}_{13} - \mathfrak{D}_{12})/S, \\ D_{21} &= Y_2 \mathfrak{D}_{13}(\mathfrak{D}_{23} - \mathfrak{D}_{12})/S, \\ D_{22} &= \mathfrak{D}_{23}(Y_2 \mathfrak{D}_{13} + (1 - Y_2) \mathfrak{D}_{12})/S, \end{aligned}$$

where  $Y_k = C_k/C$  are the mole fractions and  $S = Y_1 \mathfrak{D}_{23} + Y_2 \mathfrak{D}_{13} + Y_3 \mathfrak{D}_{12}$ . Notice that Equation (13) reduces to the standard binary diffusion model (or Fick's law) when the number of components  $n_c = 2$ .

## ACKNOWLEDGEMENTS

We are grateful to Radu Bradean (Simon Fraser University) and Huaxiong Huang (York University) for many helpful discussions. We are also indebted to John Kenna and Greg James of Ballard Power Systems their support and encouragement, and for their willingness to provide experimental data.

## REFERENCES

1. K. A. Akanni, J. W. Evans, and I. S. Abramson. Effective transport coefficients in heterogeneous media. *Chem. Engrg. Sci.*, 42(8):1945–1954, 1987.
2. S. Amali, D. E. Rolston, and T. Yamaguchi. Organic chemicals in the environment: Transient multicomponent gas-phase transport of volatile organic chemicals in porous media. *J. Environ. Qual.*, 25:1041–1047, 1996.

3. N. R. Amundson, E. Morano, and R. Sanders. Techniques for the numerical solution of steady reaction–diffusion systems employing Stefan–Maxwell diffusion. *East–West J. Numer. Math.*, 6(1):9–25, 1998.
4. H. D. Baehr and K. Stephan. *Heat and Mass Transfer*. Springer-Verlag, Berlin, 1998.
5. J. Bear and Y. Bachmat. *Introduction to Modeling of Transport Phenomena in Porous Media*. Kluwer Academic, Dordrecht, 1990.
6. A. L. Chernyakov. Fluid flow through three-dimensional fibrous porous media. *J. Exp. Theor. Phys. (transl. of Zh. Éksp. Teor. Fiz.)*, 86(6):1156–1166, 1998.
7. R. E. Ewing, J. Wang, and S. L. Weekes. On the simulation of multicomponent gas flow in porous media. *Appl. Numer. Math.*, 31(4):405–428, 1999.
8. J.-M. Fiard and R. Herbin. Comparison between finite volume and finite element methods for an elliptic system arising in electrochemical engineering. *Comput. Methods Appl. Mech. Engrg.*, 115:315–338, 1994.
9. V. Gurau, H. Liu, and S. Kakaç. Two-dimensional model for proton exchange membrane fuel cells. *AIChE J.*, 44(11):2410–2422, 1998.
10. I.-M. Hsing and P. Futerko. Two-dimensional simulation of water transport in polymer electrolyte fuel cells. *Chem. Engrg. Sci.*, 55:4209–4218, 2000.
11. G. W. Jackson and D. F. James. The permeability of fibrous porous media. *Can. J. Chem. Engrg.*, 64:364–374, 1986.
12. D. L. Koch and J. F. Brady. The effective diffusivity of fibrous media. *AIChE J.*, 32(4):575–591, 1986.
13. R. Krishna. Problems and pitfalls in the use of the Fick formulation for intraparticle diffusion. *Chem. Engrg. Sci.*, 48(5):845–861, 1993.
14. R. C. Lam and J. L. Kardos. The permeability and compressibility of aligned and cross-ply carbon fiber beds during processing of composites. *Polymer & Engrg. Sci.*, 31(14):1064–1070, 1991.
15. W.-k. Lee, C.-H. Ho, J. W. Van Zee, and M. Murthy. The effects of compression and gas diffusion layers on the performance of a PEM fuel cell. *J. Power Sources*, 84:45–51, 1999.
16. O. Manley, M. Marion, and R. Temam. Fully nonlinear multispecies reaction-diffusion equations. *Appl. Math. Lett.*, 8(4):7–11, 1995.
17. D. A. Nield and A. Bejan. *Convection in porous media*, volume 229 of *Lecture Notes in Control and Information Sciences*. Springer-Verlag, New York, 2nd edition, 1998.
18. L. R. Petzold. A Description of DASSL: A Differential/Algebraic System Solver. Technical Report SAND82–8637, Sandia National Laboratories, Livermore, CA, Sept. 1982.
19. R. Peyret and T. D. Taylor. *Computational Methods for Fluid Flow*. Springer-Verlag, New York, 1983.
20. K. Promislow and J. M. Stockie. Adiabatic relaxation of convective-diffusive gas transport in a porous fuel cell electrode. *SIAM J. Appl. Math.*, 62(1):180–205, 2001.
21. D. Singh, D. M. Lu, and N. Djilali. A two-dimensional analysis of mass transport in proton exchange membrane fuel cells. *Int. J. Engrg. Sci.*, 37(4):431–452, 1999.
22. SLATEC Common Mathematical Library, Version 4.1, 1993. <http://www.netlib.org/slatec/>.
23. B. E. Sleep and J. F. Sykes. Compositional simulation of groundwater contamination by organic compounds. 1. Model development and verification. *Water Resour. Res.*, 29(6):1697–1708, 1993.
24. R. Taylor and R. Krishna. *Multicomponent Mass Transfer*. Wiley Series in Chemical Engineering. John Wiley & Sons, 1993.
25. I. W. Turner and W. J. Ferguson. An unstructured mesh cell-centered control volume method for simulating heat and mass transfer in porous media: Application to softwood drying, Part II: The anisotropic model. *Appl. Math. Modelling*, 19:668–674, 1995.
26. C. Y. Wang and P. Cheng. A multiphase mixture model for multiphase, multicomponent transport in capillary porous media—I. Model development. *Int. J. Heat Mass Transfer*, 39(17):3607–3618, 1996.
27. N. E. Wijesundera, B. F. Zheng, M. Iqbal, and E. G. Hauptmann. Numerical simulation of the transient moisture transfer through porous insulation. *Int. J. Heat Mass Transfer*, 39(5):995–1004, 1996.
28. J. S. Yi and T. V. Nguyen. Multicomponent transport in porous electrodes of proton exchange membrane fuel cells using the interdigitated gas distributors. *J. Electrochem. Soc.*, 146(1):38–45, 1999.